Journal of Materials Chemistry A

PAPER

View Article Online
View Journal | View Issue

Cite this: J. Mater. Chem. A, 2015, 3, 16263

Perpendicularly oriented few-layer $MoSe_2$ on SnO_2 nanotubes for efficient hydrogen evolution reaction†

Yunpeng Huang,[a] Yue-E Miao,[a] Jun Fu,[b] Shuyi Mo,[b] Chun Wei[b] and Tianxi Liu*[a]

Received 21st May 2015
Accepted 3rd July 2015

DOI: 10.1039/c5ta03704b

www.rsc.org/MaterialsA

Maximizing the number of exposed active edges in newly emerged two-dimensional few-layer $MoSe_2$ nanostructures is a key issue to fully realize the excellent electrochemical properties of $MoSe_2$. In this work, a SnO_2@$MoSe_2$ nanostructure was successfully fabricated through a facile electrospinning technique combined with sintering and a solvothermal method. This rationally designed hierarchical architecture has perpendicularly oriented few-layered $MoSe_2$ nanosheets uniformly and fully covering both inner and outer surfaces of SnO_2 nanotubes, which exhibits excellent electrochemical activity as a hydrogen evolution reaction (HER) catalyst with a small onset potential of −0.11 V *vs.* reversible hydrogen electrode (RHE) and a small Tafel slope of 51 mV per decade. This excellent performance may originate from the unique hierarchical tubular structure with fully exposed active edges and open spaces for fast electron/electrolyte transfer, enabling their potential to replace Pt as a future electrocatalyst in HER.

Introduction

Increasing demands for sustainable energy calls for innovation on energy conversion technology. Among various renewable energy alternatives, hydrogen is considered as a promising candidate to replace fossil fuels as a future energy carrier due to its highest energy density and environmental friendliness.[1,2] Electrochemical production of hydrogen from water splitting is a widely adopted method that mainly relies on the catalytic activity of hydrogen evolution reaction (HER) catalysts.[3] Platinum (Pt) and its alloys are the best-known HER catalysts due to their excellent catalytic activity,[4,5] while their low abundance and high cost severely hinder the massive applications of these catalysts. Thus, alternative HER catalysts based on earth-abundant materials with high activity are highly desirable and being vigorously pursued.[6–8]

Recently, layered transition metal dichalcogenides (LTMD) have received much research attention in energy conversion and storage fields due to their tunable band structure and intrinsic electrochemical properties,[9–17] whose crystal structures are built up of strongly covalently bonded X–M–X (M = Mo, W, *etc.*; X = S, Se, and Te) single layers by van der Waals forces, like graphite.[18,19] For instance, few-layered MoS_2 and WS_2 nanosheets have been reported as high-performance catalysts for electrochemical HER in terms of high catalytic activity and long term stability, with the HER mechanism demonstrated by the interplay between theoretical calculations and experiments.[9,10,14,20,21] $MoSe_2$, a typical layered LTMD semiconducting material, has also captured much attention recently due to its more metallic nature compared with MoS_2, which leads to the higher electrical conductivity endowing itself as a novel HER catalyst.[22–24] Previous studies show that the unsaturated Se-edges in $MoSe_2$ nanosheets are electrocatalytically active, which is in favor of the HER process as S-edges in MoS_2.[25,26] Theoretical calculation even reveals that the Gibbs free energy for hydrogen adsorption onto $MoSe_2$ edges is lower than that of MoS_2, resulting in higher coverage of hydrogen adsorption.[27] Cui *et al.* reported the synthesis of $MoSe_2$ thin films on Si substrates with vertically aligned layers and largely exposed edges *via* a high-temperature selenization process, and demonstrated that the HER catalytic activity of $MoSe_2$ films correlates directly with the density of exposed active edges.[26] Chen and coworkers successfully prepared perpendicularly oriented $MoSe_2$ nanosheets on a graphene network through a CVD method, which enhanced the exposed active sites and improved electron transfer between the catalyst and the electrode, thus resulting in a small overpotential of 0.159 V at a current density of 10 mA cm^{-2} with a decreased Tafel slope of 61 mV per decade.[28] Therefore, two basic ways should be taken into account to improve the HER activity of $MoSe_2$: (1) increasing the density of active sites or exposed edges of the

[a]State Key Laboratory of Molecular Engineering of Polymers, Department of Macromolecular Science, Fudan University, Shanghai, 200433, P. R. China. E-mail: txliu@fudan.edu.cn

[b]Key Laboratory of New Processing Technology for Nonferrous Metals and Materials, Ministry of Education, College of Materials Science and Engineering, Guilin University of Technology, Guilin, 541004, China

† Electronic supplementary information (ESI) available: Low magnification SEM images of $SnCl_2$/PVP precursor nanofibers, SnO_2 nanotubes and SnO_2@$MoSe_2$-3 hybrids; SEM image of pure $MoSe_2$ nanospheres; EDS spectrum of the SnO_2@$MoSe_2$-3 hybrid; nitrogen adsorption/desorption isotherms; morphology of the SnO_2@$MoSe_2$-3 composite after 3000 CV cycles. See DOI: 10.1039/c5ta03704b

catalyst; (2) enhancing the electrical contact to active sites by decreasing the number of $MoSe_2$ layers and constructing hybrids with other conductive substrates.

SnO_2 is a well-known transition metal oxide semiconductor which holds unique electrochemical properties like large band gap (3.6 eV) and high optical transparency, making it a promising material for gas sensors, transparent electrodes and other optoelectronic devices.[29–33] Interestingly, SnO_2 nanotubes composed of nanosized subunits can be facilely obtained through direct sintering of electrospun polymeric nanofibers containing SnO_2 precursors, which possess a high surface area and numerous active sites.[34] Our previous work on the fabrication of MoS_2 nanosheet coated SnO_2 composites indicates the great potential of electrospun SnO_2 nanotubes as a perfect support for synthesis of hierarchical structures with synergistically enhanced electrochemical activity.[21] In the present work, perpendicularly oriented few-layer $MoSe_2$ nanosheets are successfully grown on both inner and outer sides of electrospun SnO_2 nanotubes by a low-temperature solvothermal method. On the one hand, rough and tubular SnO_2 nanotubes can direct the uniform formation and distribution of few-layer $MoSe_2$ nanosheets, thus maximizing the number of exposed active edges to protons and facilitating ion/electrolyte transport. On the other hand, electron transfer efficiency at the electrode interface can be greatly promoted through the interconnected SnO_2 nanotubes. This rationally synthesized SnO_2@$MoSe_2$ hybrid exhibits significantly improved catalytic activity for the HER with a lower onset potential and smaller Tafel slope compared with pure $MoSe_2$ nanosheets and its MoS_2 counterparts.

Experimental

Materials

Polyvinylpyrrolidone (PVP, M_w = 1 300 000 g mol^{-1}) was obtained from Sigma-Aldrich. Selenium powder (Se, 99.99%), Na_2MoO_4 (99.99%), hydrazine hydrate ($N_2H_4 \cdot H_2O$, 50 wt% in water) and $SnCl_2 \cdot 2H_2O$ (99.99%) were provided by Sinopharm Chemical Reagent Co. Ltd. Pt/C catalyst (20 wt% platinum on carbon black) was purchased from Alfa Aesar. *N*,*N*-Dimethylformamide (DMF) and ethanol were obtained from Shanghai Chemical Reagent Company. All aqueous solutions were prepared with doubly distilled water.

Synthesis of SnO_2@$MoSe_2$ hybrids

The preparation procedure of SnO_2@$MoSe_2$ hybrids is schematically described in Scheme 1. SnO_2 nanotubes were first synthesized according to a versatile sol–gel electrospinning technique combined with subsequent sintering as reported in our previous work.[21] Typically, 1 g of $SnCl_2 \cdot 2H_2O$ and 1.2 g of PVP were dissolved in a mixture of 5 mL of ethanol and 5 mL of DMF at room temperature under vigorous stirring to form the electrospinning solution. The viscous transparent solution was then transferred into a 5 mL plastic syringe and injected with a feeding rate of 0.25 mm min^{-1} through a no. 21 stainless steel needle positioned 15 cm away from an aluminum drum collector. When a fixed voltage of 20 kV was applied to the system, $SnCl_2$/PVP composite nanofibers were generated and deposited on the drum in a manner of self-standing non-woven membranes. After sintering for 3 h at 600 °C in air, PVP was decomposed, meanwhile, SnO_2 crystallized to form a tubular structure. The as-prepared SnO_2 nanotubes were ground and pre-treated in 10% HCl solution to remove any impurities. For the solvothermal process, a 5 mg mL^{-1} Se solution was first prepared in a flask by adding a certain amount of Se powder into hydrazine hydrate solution. The colorless solution soon turned dark brown after 1 h of magnetic stirring at 80 °C oil bath. In a separate flask, 20 mg SnO_2 nanotubes were dispersed in 10 mL DMF under sonication for at least 20 min, then a stoichiometric amount of Na_2Mo_4 was added to the dispersion and sonicated for another 10 min. Afterwards, 10 mL of Se solution was added dropwise into the above dispersion with the final Mo : Se molar ratio of 1 : 2. The mixture was transferred to a 40 mL Teflon-lined autoclave and heated in an oven at 180 °C for 12 h. After natural cooling, black precipitates were obtained and washed with de-ionized water for several times. After drying overnight, the precipitates were annealed in N_2 at 450 °C with a ramp rate of 5 °C min^{-1} for 2 h to yield a crystallized SnO_2@$MoSe_2$ hybrid. Pure $MoSe_2$ was also produced *via* the above method without addition of SnO_2 nanotubes.

Characterization

The morphology of the samples was observed using a field emission scanning electron microscope (FESEM, Zeiss) at an acceleration voltage of 5 kV. Transmission electron microscopy (TEM) was performed under an acceleration voltage of 200 kV with a Tecnai G2 20 TWIN TEM. Thermogravimetric analysis (Pyris 1 TGA) was performed under an air flow from 100 to 800 °C at a heating rate of 20 °C min^{-1}. X-ray diffraction (XRD) experiments were conducted from $2\theta = 10°$ to 80° on an X'Pert Pro X-ray diffractometer with Cu Kα radiation ($\lambda = 0.1542$ nm) under a voltage of 40 kV and a current of 40 mA. X-ray photoelectron spectroscopy (XPS) analyses were made with a Thermo Scientific ESCALAB 250Xi using an Al Kα source 1846.6 eV anode. All XPS spectra were corrected using the C 1s line at 285 eV. Curve fitting and background subtraction were accomplished using XPS PEAK41 software. The Brunauer–Emmett–Teller (BET) method was utilized to calculate the specific surface area. Using the Barrett–Joyner–Halenda (BJH) model, pore volumes and pore-size distributions were derived from the adsorption branches of isotherms, while the total pore volumes were estimated from the adsorbed amount at a relative pressure P/P_0 of 0.989. The calibration curve was obtained using carbon black (part no. 004-16833-00) as the reference material and N_2 as the adsorption gas.

Electrochemical measurements

Prior to all electrochemical measurements, a glassy carbon electrode (GCE) was sequentially polished with 1.0, 0.3 and 0.05 μm alumina slurries, and then ultrasonicated in a mixed solution of deionized water and ethanol (weight ratio = 1 : 1) for 5 min. Afterwards, the electrode was left to dry under a N_2 stream. Then, 2 mg of SnO_2@$MoSe_2$ hybrids was dispersed in

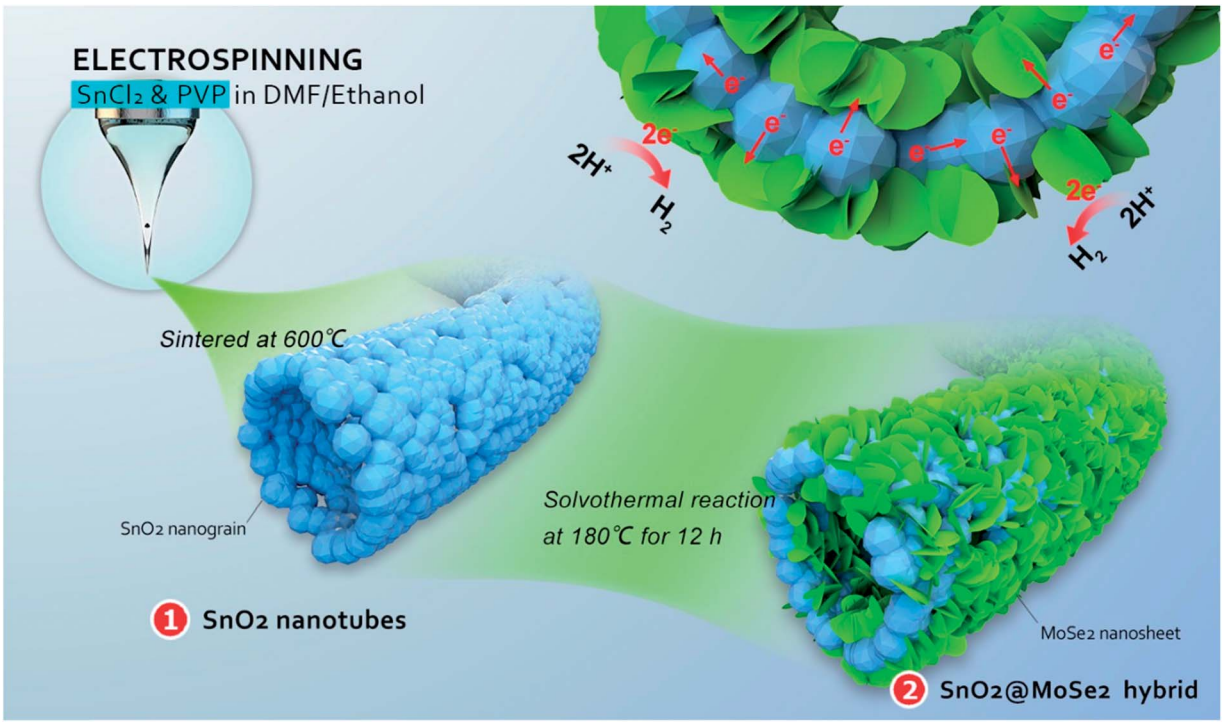

Scheme 1 A schematic illustration of the preparation of an SnO_2@$MoSe_2$ hybrid.

1 mL of water along with 20 μL Nafion (5 wt% in ethanol) for at least 15 min sonication to form a homogeneous emulsion. Finally, 10 μL of the above slurry was dropped onto the GCE with a diameter of 3 mm to form the SnO_2@$MoSe_2$ modified GCE. For comparison, neat SnO_2 nanotubes, pure $MoSe_2$ and the commercially available Pt/C modified electrodes were also prepared in the same way.

All electrochemical studies were performed in a standard three-electrode setup using a CHI 660D electrochemical workstation (Shanghai Chenhua Instrument Co., China), where a platinum wire was used as the counter electrode, a saturated calomel electrode (SCE) as the reference electrode and the modified GCE as the working electrode. The final potential was calibrated to the reversible hydrogen electrode (RHE) by adding a value of (0.241 + 0.059 pH) V for all the electrochemical tests. The electrocatalytic activity of the SnO_2@$MoSe_2$ hybrid catalyst towards HER was examined using liner sweep voltammetry (LSV) in nitrogen purged 0.5 M H_2SO_4 with a scan rate of 2 mV s^{-1} at room temperature. AC impedance measurements were carried out in 0.5 M H_2SO_4 from 10^{-2} to 10^6 Hz with an AC amplitude of 5 mV.

Results and discussion

Morphology and structure of SnO_2@$MoSe_2$ hybrids

Electrospinning is a simple and versatile method for fabricating polymer nanofibers as well as ceramic one-dimensional (1D) nanostructures. As shown in Fig. S1,† uniformly generated $SnCl_2$/PVP precursor nanofibers with smooth surfaces and random orientations can be clearly observed. After being treated at 600 °C to burn out the PVP component, SnO_2 nanotubes can be simultaneously formed during high temperature annealing according to the Kirkendall effect.[35] Fig. S2† reveals the networked SnO_2 nanotubes with a well-defined tubular structure and rough texture. Notably, the obtained SnO_2 nanotubes are composed of SnO_2 nanograins with a mean diameter of 50 nm (Fig. 1A). This unique figuration will undoubtedly increase the surface area and the number of active sites, resulting from the synthesis of hierarchical structures.

A facile low-temperature solvothermal process combined with post annealing treatment was utilized here to deposit crystallized $MoSe_2$ nanosheets on SnO_2 nanotubes. In this work, different concentrations of Se solution (1 mg mL^{-1}, 3 mg mL^{-1} and 5 mg mL^{-1}) were prepared to adjust the loading amount of $MoSe_2$, with the corresponding products denoted as SnO_2@$MoSe_2$-1, SnO_2@$MoSe_2$-3 and SnO_2@$MoSe_2$-5, respectively. As shown in Fig. 1B, only a few inconspicuous flakes of $MoSe_2$ are scattered on SnO_2 nanotubes under low Se dosage. For the SnO_2@$MoSe_2$-3 hybrid (Fig. 1C and S3†), $MoSe_2$ subunits with a curled shape and perpendicular orientation are evenly distributed on both outer and inner surfaces of SnO_2 nanotubes, which also interconnect with each other to form an open structure for electrolyte permeation. This unique tubular architecture can provide numerous exposed active edges and shortened pathways for ion and electron transfer, which will potentially lead to enhanced electrocatalytic activity. Further increasing the Se concentration (Fig. 1D), $MoSe_2$ nanosheets tend to agglomerate with each other which largely destroy the open structure. Worse still, the cavities of SnO_2 nanotubes are also blocked by $MoSe_2$ aggregations, which will surely

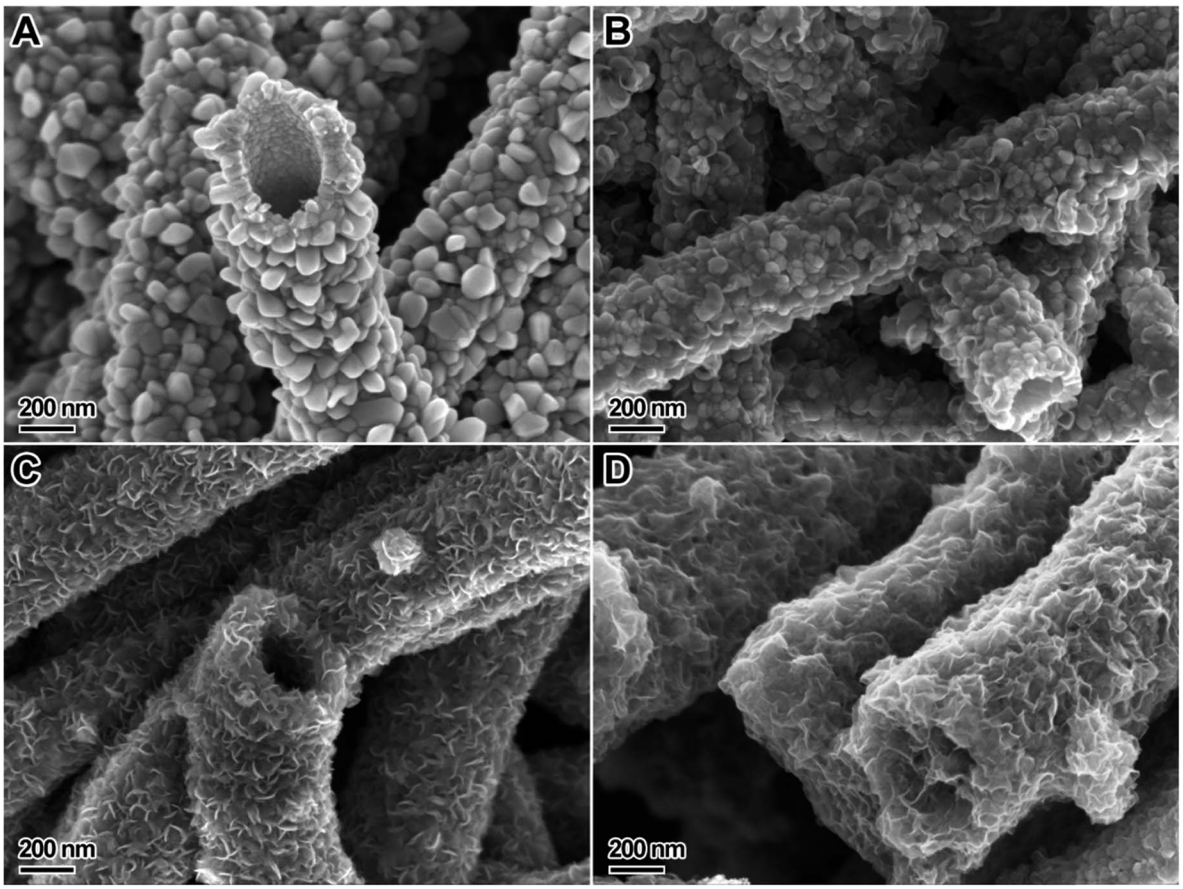

Fig. 1 FESEM images of (A) neat SnO_2 nanotubes, (B) SnO_2@$MoSe_2$-1, (C) SnO_2@$MoSe_2$-3, and (D) SnO_2@$MoSe_2$-5 hybrids.

deteriorate the overall electrochemical performance. As shown in Fig. S4,† pure $MoSe_2$ produced in the absence of SnO_2 presents a wrinkled spherical morphology. Fig. 2 shows the typical TEM images of an SnO_2@$MoSe_2$-3 hybrid. It can be clearly observed that $MoSe_2$ nanosheets are grown uniformly on SnO_2 nanotubes to form a 1D hierarchical tubular structure (Fig. 2A). In addition, the thickness of the nanosheets is ultrathin as observed from the sharp contrast in Fig. 2B. An individual sheet is composed of 4–6 layers of $MoSe_2$ with an interlayer spacing of 0.62 nm, which matches well with the (002) lattice spacing of $MoSe_2$. All these morphological characterization experiments give a visual confirmation on the successful synthesis of few-layer $MoSe_2$ nanosheets on both outer and inner surfaces of SnO_2 nanotubes.

The crystal structures of as-synthesized pure $MoSe_2$ and SnO_2@$MoSe_2$-3 hybrids were studied using XRD as shown in Fig. 3. A series of diffraction peaks can be observed from curve A, which is ascribed to the highly crystalline rutile structure of SnO_2 nanotubes (JCPDF, card no. 77-0450). As for pure $MoSe_2$ (Fig. 3B), the detected peaks at $2\theta = 13.7^\circ$, 26.4°, 32.2°, 37.3°, 53.8°, 56.4°, 60.9° and 67.0° can be readily indexed to the (002), (004), (100), (103), (106), (008), (107) and (202) diffraction planes of the hexagonal 2H-$MoSe_2$ phase (JCPDF card, no. 87-2419), respectively, revealing the high purity of synthesized $MoSe_2$. As for the SnO_2@$MoSe_2$-3 hybrid, diffraction peaks of (002), (100) and (103) can be clearly observed, indicating the successful growth of $MoSe_2$ on SnO_2 nanotubes while the invisibility of other diffraction peaks belonging to $MoSe_2$ may be ascribed to the much higher intensity of SnO_2 diffraction peaks. In order to further determine the elemental composition and oxidation state of the SnO_2@$MoSe_2$-3 hybrid, XPS analysis is presented in Fig. 4. Characteristic peaks of Mo, Se, Sn, O, and C elements are indicated in the survey spectrum (Fig. 4A), which is in good agreement with the EDS results (Fig. S5†). The C element may result from the residual carbon-based contaminants. The high-resolution spectrum of Mo 3d reveals two major peaks at 228.9 and 232.1 eV assigned to Mo $3d_{5/2}$ and Mo $3d_{3/2}$ orbitals, repectively, confirming that Mo is in its Mo(IV) state. Meanwhile, the binding energies of Se $3d_{5/2}$ and Se $3d_{3/2}$ at 54.5 and 55.2 eV, along with Se $3p_{3/2}$ and Se $3p_{1/2}$ at 160.8 and 166.6 eV, all indicate the -2 oxidation chemical state of Se.[22,23,27] Moreover, the detailed compositional analysis reveals that the surface Mo : Se atomic ratio is 9 : 21, which is close to the formula of $MoSe_2$.

To further determine the loading percentage of $MoSe_2$ in the hybrids, TGA was conducted under air flow as shown in Fig. 5. Ceramic SnO_2 nanotubes do not show any weight change as expected, while pure $MoSe_2$ undergoes a 10% weight increment between 336 °C and 371 °C, which is in accordance with the results in the previously reported work.[36] This can be explained as follows. At a relatively low temperature of 336 °C, $MoSe_2$

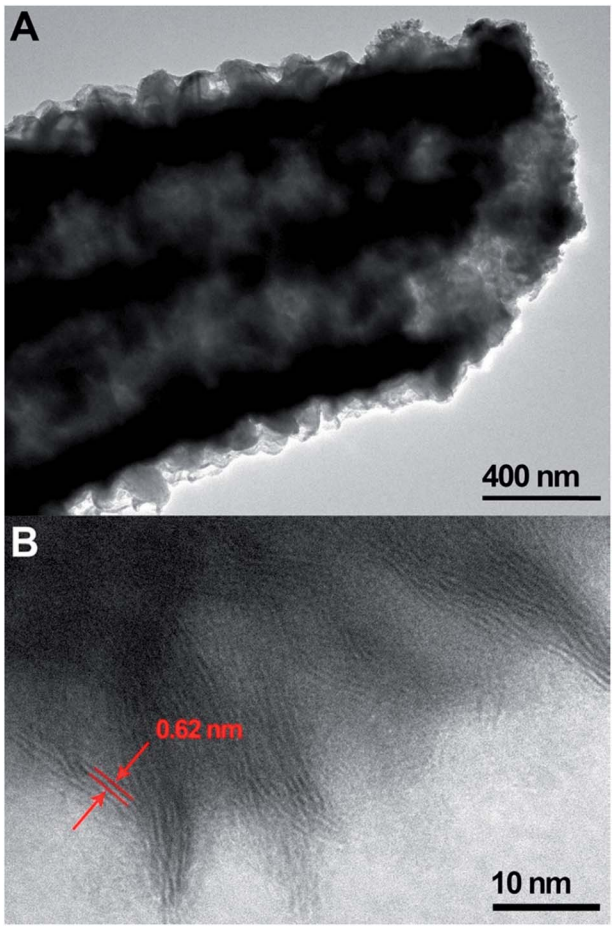

Fig. 2 TEM images of the SnO_2@$MoSe_2$-3 hybrid at (A) low and (B) high magnifications.

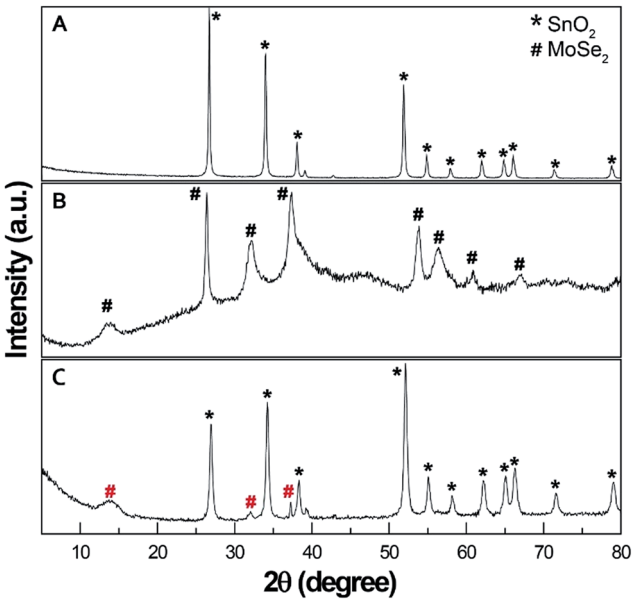

Fig. 3 XRD patterns of (A) neat SnO_2 nanotubes, (B) pure $MoSe_2$ nanospheres, and (C) SnO_2@$MoSe_2$-3 hybrid.

starts to pyrolyse according to $2MoSe_2 + 7O_2 = 2MoO_3 + 4SeO_2$, resulting in solid-state SeO_2 and thus leading to the total weight increment. As temperature reaches the sublimation temperature of SeO_2, *i.e.* 371 °C, SeO_2 starts to volatilize and the total weight decreases. The final residue of MoO_3 accounts for 57.4% of the initial weight, in accordance with the stoichiometric value. Based on the TGA curves, the loading percentage of $MoSe_2$ on SnO_2 is calculated to be 12.9%, 43.9% and 66.0% for SnO_2@$MoSe_2$-1, SnO_2@$MoSe_2$-3, and SnO_2@$MoSe_2$-5 hybrids, respectively. This pretty high loading amount of $MoSe_2$ nanosheets is probably due to the inner and outer double-surface of the rough and beaded SnO_2 nanotubes, which provides substantial nucleation sites for the growth of $MoSe_2$ nanosheets. Notably, all SnO_2@$MoSe_2$ hybrids undergo an indistinctive weight gain between 336 °C and 371 °C compared with that of pure $MoSe_2$, which may be attributed to the rapid heat transfer and gaseous volatilization facilitated by the open structure of interconnected few-layer $MoSe_2$ nanosheets.

In order to discuss the textural information of SnO_2@$MoSe_2$ composites with different $MoSe_2$ coverage, Brunauer–Emmett–Teller (BET) analyses were conducted with the N_2 adsorption/desorption isotherms and pore size distribution diagrams shown in Fig. S6.† Table S1† presents the exact surface data of the composites, that SnO_2@$MoSe_2$-3 has the highest specific surface area of 57.8 $m^2\ g^{-1}$, whereas SnO_2@$MoSe_2$-5 shows a reduced surface area of 36.3 $m^2\ g^{-1}$. Possible explanations for this trend can be deduced from the morphological differences (Fig. 1B–D) that SnO_2@$MoSe_2$-3 shows the most uniform distribution of $MoSe_2$ nanosheets with full coverage and perpendicular orientation compared to the other two samples, which would definitely lead to an enhanced surface area. On the other hand, an excess growth of $MoSe_2$ on SnO_2@$MoSe_2$-5 will possibly damage the porous structures by forming aggregations and blocking the channels of SnO_2 nanotubes. The minimum pore diameter (1.9 nm) and maximum cumulative adsorption pore volume (0.225 $cm^3\ g^{-1}$) also confirm the optimal textural

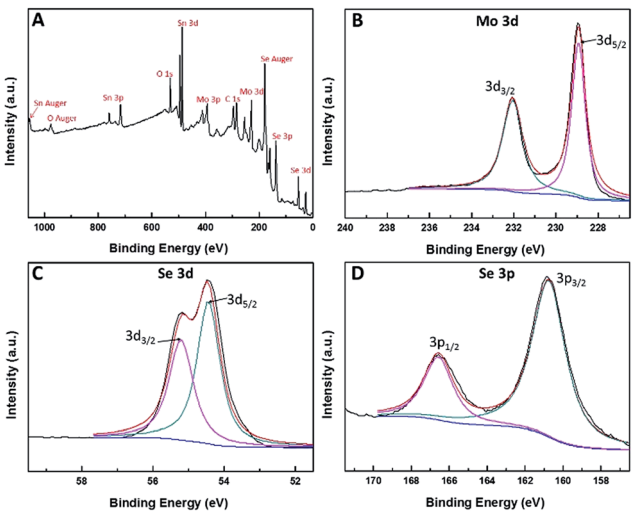

Fig. 4 XPS spectra of the SnO_2@$MoSe_2$-3 hybrid: (A) survey spectrum, (B) Mo 3d, (C) Se 3d, and (D) Se 3p.

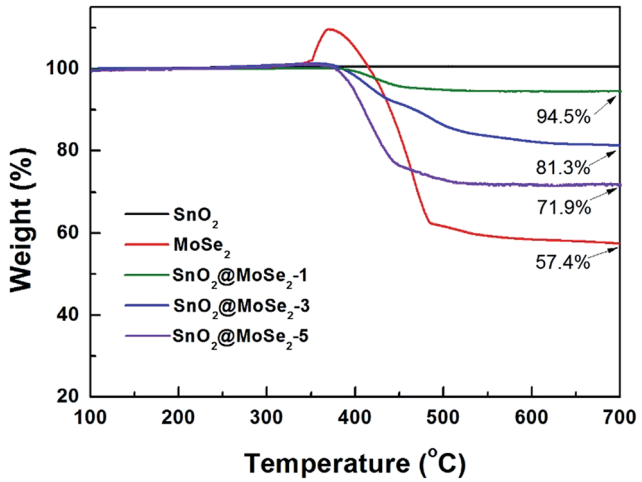

Fig. 5 TGA tests for neat SnO_2 nanotubes, pure $MoSe_2$ nanospheres and SnO_2@$MoSe_2$ hybrids.

properties of SnO_2@$MoSe_2$-3, which will potentially benefit the electrochemical performance as an HER catalyst.

Electrochemical evaluation of an HER catalyst

The electrocatalytic HER activity of SnO_2@$MoSe_2$ hybrid materials deposited on the GCE was investigated in 0.5 M H_2SO_4 solution using a typical three-electrode setup. Generally speaking, an optimal HER catalyst is a material that could give the highest current at the lowest overpotential, as well as a low HER onset potential (*i.e.*, the potential at which HER activity begins) comparable to that of a Pt catalyst. The Tafel slope, which can be deduced from the Tafel equation ($\eta = b\log(j) + a$, where η is the overpotential, j is the current density and b is the Tafel slope), is always correlated with the reaction pathway and the adsorption type.

First of all, the electrochemical activities of SnO_2@$MoSe_2$ hybrids with different loading percentages were measured for a direct comparison (Fig. 6). The LSV curve of the SnO_2@$MoSe_2$-1 modified GCE shows an onset potential of about −0.16 V *vs.* RHE, while the curve of the SnO_2@$MoSe_2$-3 hybrid is more positive with a lower onset potential of about −0.11 V. As for the SnO_2@$MoSe_2$-5 modified GCE, its LSV curve is negatively shifted exhibiting decreased activity. Moreover, the SnO_2@$MoSe_2$-3 hybrid exhibits a current density of 10 mA cm^{-2} at a lower overpotential of 0.174 V which is much smaller than those of SnO_2@$MoSe_2$-1 (10 mA cm^{-2} at 0.247 V) and SnO_2@$MoSe_2$-5 (10 mA cm^{-2} at 0.190 V) and is also outstanding among the MoS_2- or $MoSe_2$-based HER catalysts (detailed comparison between different catalysts is provided in Table 1). Possible reasons for different HER activity can be deduced from the BET analyses (Fig. S6, Table S1†) and morphological difference (Fig. 1B and C), the SnO_2@$MoSe_2$-1 hybrid has a much less $MoSe_2$ coating than SnO_2@$MoSe_2$-3, while the overloaded SnO_2@$MoSe_2$-5 aggregates severely block the open structure for ion/electrolyte transfer. Moreover, the SnO_2@$MoSe_2$-3 hybrid exhibits the highest surface area and largest pore volume compared to SnO_2@$MoSe_2$-1 and SnO_2@$MoSe_2$-5 hybrids. In this regard, the SnO_2@$MoSe_2$-3 hybrid shows the optimized hierarchical structure with more uniform distribution of $MoSe_2$ nanosheets and exposed much more active edges, thus leading to the highest HER catalytic activity.

Further comparison between neat SnO_2 nanotubes, pure $MoSe_2$, a physical mixture of SnO_2 and $MoSe_2$ (denoted as SnO_2 & $MoSe_2$), the SnO_2@$MoSe_2$-3 hybrid and commercially available Pt/C catalyst was also performed. As presented in Fig. 7A, the Pt/C modified GCE exhibits extremely high HER catalytic activity with a near zero onset potential and large current density. In contrast, neat SnO_2 nanotubes show almost no HER activity with a near horizontal line within the potential window. Pure $MoSe_2$ and SnO_2 & $MoSe_2$ exhibit distinctive electrochemical HER activity owing to the intrinsic HER activity of LTMD, but still a much lower anodic current and more negative onset potential compared with the SnO_2@$MoSe_2$-3 hybrid. This can be attributed to the insufficient exposed edges and imperfect coupling between SnO_2 and $MoSe_2$, thus leading to the weak activity of $MoSe_2$ and SnO_2 & $MoSe_2$. The outperformed HER catalytic activity of the SnO_2@$MoSe_2$-3 hybrid suggests the successful design of this tubular hierarchical architecture, which integrates the advantages of both components in a reasonable manner to achieve synergistically enhanced performance. In addition, the linear part of the Tafel plots was fitted to the Tafel equation (Fig. 7B), yielding Tafel slopes of about 70, 51 and 35 mV per decade for the pure $MoSe_2$, SnO_2@$MoSe_2$-3 hybrid and Pt/C, respectively. Therefore, the small Tafel slope of the SnO_2@$MoSe_2$-3 hybrid means a faster increment of the HER rate with increasing overpotential, which is favorable for practical applications. Additionally, with the Tafel slope of 51 mV per decade, the HER process of the SnO_2@$MoSe_2$-3 hybrid catalyst follows the Volmer–Heyrovsky or the Volmer–Tafel mechanism with the Volmer reaction as the rate-determining step.[21]

To understand the electrochemical behavior of electrodes under HER operating circumstances, electrochemical

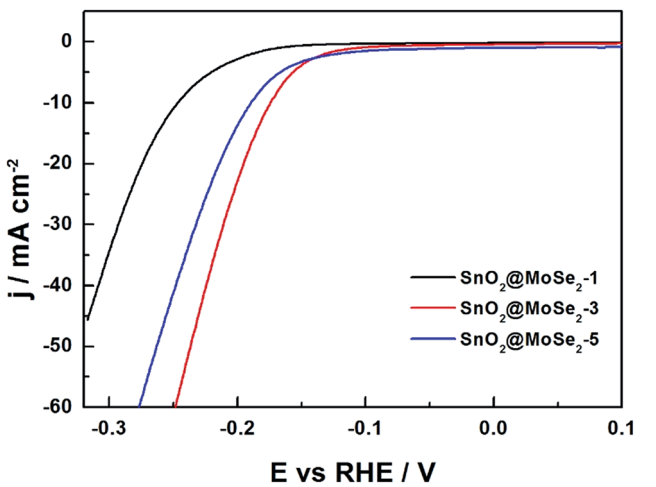

Fig. 6 LSV polarization curves of SnO_2@$MoSe_2$-1, SnO_2@$MoSe_2$-3 and SnO_2@$MoSe_2$-5 modified GCE in N_2-purged 0.5 M H_2SO_4 solution. Scan rate: 2 mV s^{-1}.

Table 1 A comparison on the HER performance between different materials

Catalyst	Synthesis method	Electrolyte	Onset potential (V *vs.* RHE)	Overpotential (V *vs.* RHE) at 10 mA cm^{-2}	Tafel slope (mV per decade)	Ref.
SnO_2@$MoSe_2$	Solvothermal	0.5 M H_2SO_4	−0.11	0.174	51	This work
S-doped $MoSe_2$	Reflux method	0.5 M H_2SO_4	−0.09	~0.10	60	22
$MoSe_{2-x}$ ($x \sim 0.47$)	Colloidal synthesis	0.5 M H_2SO_4	−0.17	~0.28	98	23
$MoSe_2$	CVD	0.5 M H_2SO_4	−0.2	>0.4	105–120	26
$MoSe_2$	CVD	0.5 M H_2SO_4	−0.11	0.25	59.8	25
$MoSe_2$/rGO	Hydrothermal	0.5 M H_2SO_4	−0.05	0.15	69	27
MoS_2/SnO_2	Solvothermal	0.5 M H_2SO_4	−0.15	~0.22	59	21
Exfoliated MoS_2	Ultrasonication	0.5 M H_2SO_4	−0.12	~0.21	70	37

impedance spectroscopy (EIS) tests were conducted for the pure $MoSe_2$, SnO_2@$MoSe_2$-3 hybrid and Pt/C. The inset of Fig. 8A presents the equivalent circuit model to illustrate the performance of the electrodes, where R_{ct} represents the charge transfer resistance, R_s is the series resistance, and CPE indicates the constant phase element. As shown in Fig. 8A, the visible semicircles of Nyquist plots are mainly due to the R_{ct} of H^+ reduction at the electrode–electrolyte interface. In addition, R_s can be obtained according to the *x*-intercept of Nyquist plots. Obviously, R_{ct} of the SnO_2@$MoSe_2$-3 hybrid is lower than that of neat SnO_2, indicating that the open structure and larger surface area of the SnO_2@$MoSe_2$-3 hybrid significantly decrease the ion transfer resistance along the electrode–electrolyte interface. Furthermore, the smaller R_s of the SnO_2@$MoSe_2$-3 hybrid with respect to pure $MoSe_2$ nanospheres implies that the uniform distribution of perpendicularly oriented few-layered $MoSe_2$

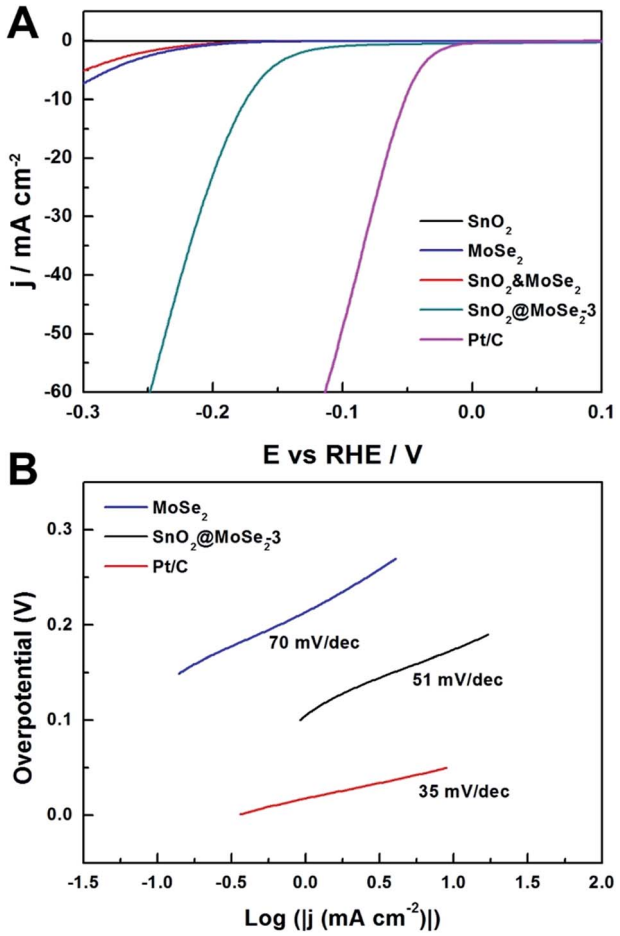

Fig. 7 (A) LSV polarization curves of the GCE modified with different materials in N_2-purged 0.5 M H_2SO_4 solution. Scan rate: 2 mV s^{-1}. (B) Tafel plots of Pt/C, pure $MoSe_2$ and SnO_2@$MoSe_2$-3 modified GCE.

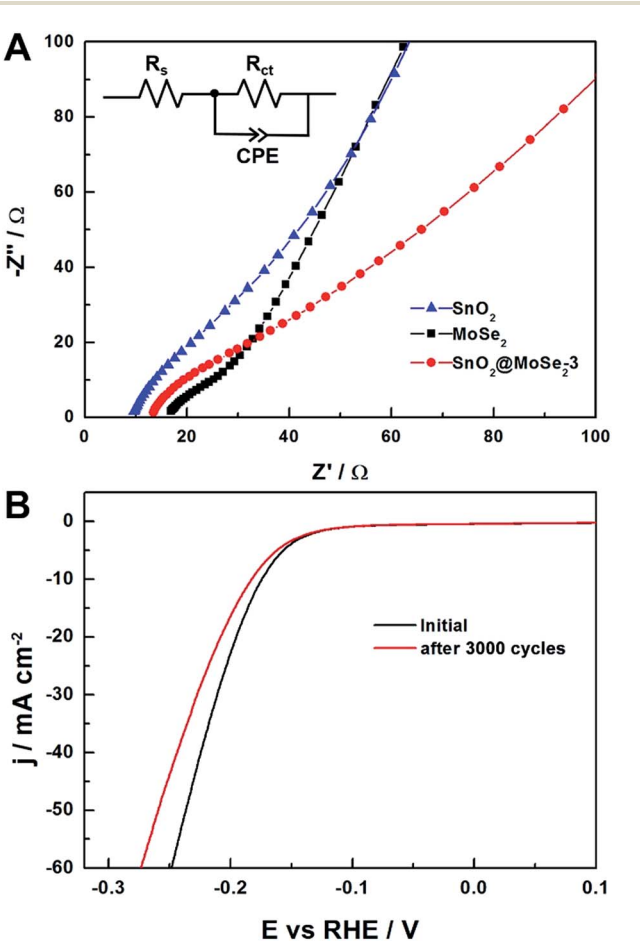

Fig. 8 (A) Nyquist plots of pure $MoSe_2$, neat SnO_2 nanotubes and the SnO_2@$MoSe_2$-3 hybrid. (B) LSV polarization curves for SnO_2@$MoSe_2$-3 modified GCE recorded before and after 3000 times of CV cycles.

nanosheets on conductive SnO_2 nanotubes could provide efficient pathways for rapid electron transfer. These pieces of analytical evidence further highlight the rational design of this hierarchical tubular SnO_2@$MoSe_2$ nanostructure.

To investigate the durability of the SnO_2@$MoSe_2$-3 modified electrode, cyclic voltammetry (CV) was conducted for 3000 cycles from −0.4 V to 0.2 V (*vs.* RHE) at 100 mV s^{-1}, and the LSV curves before and after CV tests are recorded in Fig. 8B. It can be seen that the catalyst retains the same low onset potential with slight decay in the current density, which is mainly due to the gradual accumulation of $MoSe_2$ nanosheets and decrease of the active edges as confirmed by SEM (Fig. S7†).

Conclusions

In summary, a versatile electrospinning technique combined with sintering and a low-temperature solvothermal method has been demonstrated for the successful synthesis of perpendicularly oriented few-layered $MoSe_2$ nanosheets on SnO_2 nanotubes. This rationally designed hierarchical architecture not only directs the uniform distribution of $MoSe_2$ nanosheets by virtue of the beaded SnO_2 nanotubes, but also affords efficient charge transfer pathways through the intimate interaction between the two components. The thus resulted open structure of $MoSe_2$ nanosheets with fully exposed active edges facilitates fast electrolyte diffusion and rapid electron transfer, leading to excellent HER catalytic activity with a low onset potential of −0.11 V *vs.* RHE and a small Tafel slope of 51 mV per decade. Therefore, the newly proposed protocol opens a potential avenue for the development of high-performance Pt-free HER catalysts.

Acknowledgements

The authors are grateful for the financial support from the National Natural Science Foundation of China (51125011, 51373037, 51433001), Guangxi Small Highland Innovation Team of Talents in Colleges and Universities, Guangxi Funds for Specially-appointed Expert, and Guangxi Natural Science Foundation of China (No. 2014GXNSFAA118321).

Notes and references

1 J. A. Turner, *Science*, 2004, **305**, 972–974.
2 M. S. Dresselhaus and I. L. Thomas, *Nature*, 2001, **414**, 332–337.
3 J. Greeley, T. F. Jaramillo, J. Bonde, I. Chorkendorff and J. K. Norskov, *Nat. Mater.*, 2006, **5**, 909–913.
4 B. E. Conway and B. V. Tilak, *Electrochim. Acta*, 2002, **47**, 3571–3594.
5 J. R. McKone, E. L. Warren, M. J. Bierman, S. W. Boettcher, B. S. Brunschwig, N. S. Lewis and H. B. Gray, *Energy Environ. Sci.*, 2011, **4**, 3573–3583.
6 P. Jiang, Q. Liu, Y. H. Liang, J. Q. Tian, A. M. Asiri and X. P. Sun, *Angew. Chem., Int. Ed.*, 2014, **53**, 12855–12859.
7 S. J. Peng, L. L. Li, X. P. Han, W. P. Sun, M. Srinivasan, S. G. Mhaisalkar, F. Y. Cheng, Q. Y. Yan, J. Chen and S. Ramakrishna, *Angew. Chem., Int. Ed.*, 2014, **53**, 12594–12599.
8 Y. Yang, H. L. Fei, G. D. Ruan, C. S. Xiang and J. M. Tour, *Adv. Mater.*, 2014, **26**, 8163–8168.
9 J. Lin, Z. W. Peng, G. Wang, D. Zakhidov, E. Larios, M. J. Yacaman and J. M. Tour, *Adv. Energy Mater.*, 2014, **4**, 1301875.
10 M. A. Lukowski, A. S. Daniel, F. Meng, A. Forticaux, L. S. Li and S. Jin, *J. Am. Chem. Soc.*, 2013, **135**, 10274–10277.
11 J. K. Huang, J. Pu, C. L. Hsu, M. H. Chiu, Z. Y. Juang, Y. H. Chang, W. H. Chang, Y. Iwasa, T. Takenobu and L. J. Li, *ACS Nano*, 2013, **8**, 923–930.
12 C. M. Huang, S. F. Wu, A. M. Sanchez, J. J. P. Peters, R. Beanland, J. S. Ross, P. Rivera, W. Yao, D. H. Cobden and X. D. Xu, *Nat. Mater.*, 2014, **13**, 1096–1101.
13 W. Zhou, Z. Yin, Y. Du, X. Huang, Z. Zeng, Z. Fan, H. Liu, J. Wang and H. Zhang, *Small*, 2013, **9**, 140–147.
14 L. Cheng, W. J. Huang, Q. F. Gong, C. H. Liu, Z. Liu, Y. G. Li and H. J. Dai, *Angew. Chem., Int. Ed.*, 2014, **53**, 7860–7863.
15 Q. H. Wang, K. Kalantar-Zadeh, A. Kis, J. N. Coleman and M. S. Strano, *Nat. Nanotechnol.*, 2012, **7**, 699–712.
16 A. H. Loo, A. Bonanni, Z. Sofer and M. Pumera, *Electrochem. Commun.*, 2015, **50**, 39–42.
17 Y. N. Ko, S. H. Choi, S. B. Park and Y. C. Kang, *Nanoscale*, 2014, **6**, 10511–10515.
18 G. Eda, H. Yamaguchi, D. Voiry, T. Fujita, M. W. Chen and M. Chhowalla, *Nano Lett.*, 2011, **11**, 5111–5116.
19 L. Sun, Y. L. Ying, H. B. Huang, Z. G. Song, Y. Y. Mao, Z. P. Xu and X. S. Peng, *ACS Nano*, 2014, **8**, 6304–6311.
20 S. J. Xu, D. Li and P. Y. Wu, *Adv. Funct. Mater.*, 2015, 10–1002.
21 Y. P. Huang, Y. E. Miao, L. S. Zhang, W. W. Tjiu, J. S. Pan and T. X. Liu, *Nanoscale*, 2014, **6**, 10673–10679.
22 C. Xu, S. J. Peng, C. L. Tan, H. X. Ang, H. T. Tan, H. Zhang and Q. Y. Yan, *J. Mater. Chem. A*, 2014, **2**, 5597–5601.
23 X. L. Zhou, J. Jiang, T. Ding, J. J. Zhang, B. C. Pan, J. Zuo and Q. Yang, *Nanoscale*, 2014, **6**, 11046–11051.
24 Y. F. Shi, C. X. Hua, B. Li, X. P. Fang, C. H. Yao, Y. C. Zhang, Y. S. Hu, Z. X. Wang, L. Q. Chen, D. Y. Zhao and G. D. Stucky, *Adv. Funct. Mater.*, 2013, **23**, 1832–1838.
25 H. T. Wang, D. S. Kong, P. Johanes, J. J. Cha, G. Y. Zheng, K. Yan, N. Liu and Y. Cui, *Nano Lett.*, 2013, **13**, 3426–3433.
26 D. S. Kong, H. T. Wang, J. J. Cha, M. Pasta, K. J. Koski, J. Yao and Y. Cui, *Nano Lett.*, 2013, **13**, 1341–1347.
27 H. Tang, K. P. Dou, C. C. Kaun, Q. Kuang and S. H. Yang, *J. Mater. Chem. A*, 2014, **2**, 360–364.
28 S. Mao, Z. H. Wen, S. Q. Ci, X. R. Guo, K. K. Ostrikov and J. H. Chen, *Small*, 2015, **11**, 414–419.
29 Y. E. Miao, S. X. He, Y. L. Zhong, Z. Yang, W. W. Tjiu and T. X. Liu, *Electrochim. Acta*, 2013, **99**, 117–123.
30 W. Tian, T. Y. Zhai, C. Zhang, S. L. Li, X. Wang, F. Liu, D. Q. Liu, X. K. Cai, K. Tsukagoshi, D. Golberg and Y. Bando, *Adv. Mater.*, 2013, **25**, 4625–4630.
31 B. B. Wang, X. X. Fu, F. Liu, S. L. Shi, J. P. Cheng and X. B. Zhang, *J. Alloys Compd.*, 2014, **587**, 82–89.
32 L. Renard, O. Babot, H. Saadaoui, H. Fuess, J. Brotz, A. Gurlo, E. Arveux, A. Klein and T. Toupance, *Nanoscale*, 2012, **4**, 6806–6813.

33 L. Cojocaru, C. Olivier, T. Toupance, E. Sellier and L. Hirsch, *J. Mater. Chem. A*, 2013, **1**, 13789–13799.
34 L. M. Li, X. M. Yin, S. Liu, Y. G. Wang, L. B. Chen and T. H. Wang, *Electrochem. Commun.*, 2010, **12**, 1383–1386.
35 Y. D. Yin, R. M. Rioux, C. K. Erdonmez, S. Hughes, G. A. Somorjai and A. P. Alivisatos, *Science*, 2004, **304**, 711–714.
36 Y. Liu, M. Q. Zhu and D. Chen, *J. Mater. Chem. A*, 2015, **3**, 11857–11862.
37 S. S. Ji, Z. Yang, C. Zhang, Z. Y. Liu, W. W. Tjiu, I. Y. Phang, Z. Zhang, J. S. Pan and T. X. Liu, *Electrochim. Acta*, 2013, **109**, 269–275.